A. Fani, V. Citro, F. Giannetti, F. Auteri
Computation of the Bluff-Body Sound Generation by a Self-Consistent Mean Flow Formulation
Physics of Fluids, Vol. 30, N. 3, 2018, 036102 (12 pages)
doi:10.1063/1.4997536

Computation of the bluff-body sound generation by a self-consistent mean flow formulation

A. Fani, V. Citro, F. Giannetti, and F. Auteri

Citation: Physics of Fluids **30**, 036102 (2018); doi: 10.1063/1.4997536
View online: https://doi.org/10.1063/1.4997536
View Table of Contents: http://aip.scitation.org/toc/phf/30/3
Published by the American Institute of Physics

Computation of the bluff-body sound generation by a self-consistent mean flow formulation

A. Fani,[1] V. Citro,[2,a)] F. Giannetti,[2] and F. Auteri[1]
[1]*Dipartimento di Scienze e Tecnologie Aerospaziali, Politecnico di Milano, Via La Masa 34, Milano 20156, Italy*
[2]*DIIN, Universitá degli Studi di Salerno, Via Giovanni Paolo II, 132, Fisciano 84084, Italy*

(Received 25 July 2017; accepted 2 February 2018; published online 12 March 2018)

The sound generated by the flow around a circular cylinder is numerically investigated by using a finite-element method. In particular, we study the acoustic emissions generated by the flow past the bluff body at low Mach and Reynolds numbers. We perform a global stability analysis by using the compressible linearized Navier-Stokes equations. The resulting direct global mode provides detailed information related to the underlying hydrodynamic instability and data on the acoustic field generated. In order to recover the intensity of the produced sound, we apply the self-consistent model for non-linear saturation proposed by Mantič-Lugo, Arratia, and Gallaire ["Self-consistent mean flow description of the nonlinear saturation of the vortex shedding in the cylinder wake," Phys. Rev. Lett. **113**, 084501 (2014)]. The application of this model allows us to compute the amplitude of the resulting linear mode and the effects of saturation on the mode structure and acoustic field. Our results show excellent agreement with those obtained by a full compressible simulation direct numerical simulation and those derived by the application of classical acoustic analogy formulations. *Published by AIP Publishing.*
https://doi.org/10.1063/1.4997536

I. INTRODUCTION

The flow past bluff bodies has been extensively studied for its significance in flow physics and its fundamental importance in aerodynamics, acoustics, wind engineering, and electronics cooling. Their wakes are able to generate unsteady (periodic or non-periodic) forces that can even damage structures. The flow past a circular cylinder is the prototypical configuration that captures the dominant features of bluff-body wake flows; it has received a great deal of attention and has acted as a proxy for a wide range of more complex situations.[1] It has been one of the major topics in hydrodynamics and acoustics since the first seminal work on aeolian tones made by Strouhal.[2] He performed an experimental investigation to characterize the frequency of the sound generated by the flow past a circular cylinder. The main finding was that the dimensionless number fD/U_∞, later named the "Strouhal number," is almost constant for such a kind of flow. Gerrard[3] studied the frequency and the intensity of the sound produced by the flow past circular cylinders. He recognized that the sound resulting from the production of a vortex street possesses a dipole field which consists of a dominant frequency accompanied by its harmonics.

From a theoretical point of view, Lighthill[4] laid the foundations of the theory of aerodynamic sound. He was concerned with the sound field generated by the unsteady motion of an unbounded fluid. The interaction between the fluid flow and the sound waves was not considered because of the weak feedback that exists from the acoustic field to the fluid flow. He showed that aerodynamic sound sources can be modeled as a series of monopoles, dipoles, and quadrupoles. Subsequently, Curle[5] was able to account also for the effect of solid boundaries.

From a numerical point of view, on the other hand, several techniques were developed to simulate the compressible flow past bluff bodies. It is possible to classify these approaches as follows:

(i) Semi-analytic methods: The computation of the aerodynamic source term is separated from that of the sound propagation (see, e.g., the work of Williams[6,7]).
(ii) Hybrid numerical methods: The flow field is divided into a mean and a perturbation which, in the far field, is equivalent to sound.[8]
(iii) Direct noise computation: The fluid motion and sound are computed together by solving the fully compressible equations in time.

The first group of methods are the most efficient ones, but they cannot shed light on the noise generation mechanism that characterizes each configuration. The second group, instead, uses an acoustic/viscous splitting method. This method splits the computation into two parts, but it does not use any acoustic analogy. Hardin and Pope[8] discussed the application of this method for noise computations in low Mach number flows. They represented the total flow state by an incompressible mean flow part and a perturbation about this mean flow. The first step is to solve the incompressible equations for the mean flow and then compute the perturbation field. Since this last field represents the difference between the fully compressible flow state and the incompressible one, it is linked to the acoustic quantities in the far field. However, this theory received serious criticisms in the past because of the slow decay of dilatation away from the source region.[9,10] Finally, we remark that the compressible direct numerical simulation (DNS)[11] is

a)Electronic mail: vcitro@unisa.it

the most accurate method but is also the most expensive one, especially for low Mach number computations where the CFL (Courant-Friedrichs-Lewy) condition becomes exceedingly restrictive for the large wavelength of the acoustic waves.

In this context, we discuss the application of a new method to compute the *noise intensity*, the *frequency*, and the *noise directivity* of the flow past a generic bluff body. Different from previous methods, we suggest computing these quantities by using the framework of the linear global stability analysis. Thus, we need to compute a mean flow and the inherent global modes. The amplitude of such modes, then, is computed, thanks to the method recently proposed by Mantič-Lugo *et al.*[12] They proposed a simple, self-consistent model that quantitatively predicts the saturated amplitude and flow fields. The mean flow together with the resulting most unstable eigenmode is governed by a single system of equations. Since these equations are independent of time, they allow the calculation of the mean flow approximation without requiring the integration of the time-dependent Navier-Stokes equations. The details of this approach will be given in Sec. II D.

II. THEORETICAL FRAMEWORK

A. Flow configuration and governing equations

We investigate the flow developing in the compressible regime past the circular cylinder shown in Fig. 1. It models a bluff body of diameter D placed into a uniform flow and is identical to the one investigated by Inoue and Hatakeyama.[13] The dynamics of a compressible Newtonian fluid is described in a Cartesian frame of reference (see Fig. 1). In particular, we consider a gas with a Prandtl number $Pr = \mu c_p/\kappa$ equal to 0.7, where c_p is the constant specific heat, κ is the thermal conductivity, and μ is the dynamic viscosity.

The fluid motion is described by the velocity field $\boldsymbol{u}(\boldsymbol{x}, t)$, the pressure $p(\boldsymbol{x}, t)$, the fluid density field $\rho(\boldsymbol{x}, t)$, and the temperature $T(\boldsymbol{x}, t)$ which satisfy the unsteady compressible Navier-Stokes equations,

$$\frac{\partial \rho}{\partial t} + \mathbf{u}\cdot\nabla\rho + \rho\nabla\cdot\mathbf{u} = 0, \tag{1a}$$

$$\rho\frac{\partial \mathbf{u}}{\partial t} + \rho\mathbf{u}\cdot\nabla\mathbf{u} + \nabla p - \frac{1}{Re}\nabla\cdot\tau(\mathbf{u}) = 0, \tag{1b}$$

$$\rho\frac{\partial T}{\partial t} + \rho\mathbf{u}\cdot\nabla T + (\gamma-1)\rho T\nabla\cdot\mathbf{u} - \gamma(\gamma-1)\frac{M^2}{Re}\tau(\mathbf{u}) : \mathbf{d}(\mathbf{u}) - \frac{\gamma}{Pr\,Re}\nabla^2 T = 0, \tag{1c}$$

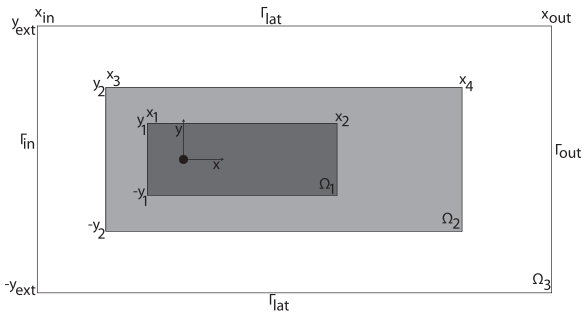

FIG. 1. Mesh structure for the cylinder flow.

$$\rho T - 1 - \gamma M^2 p = 0, \tag{1d}$$

where γ is the ratio of specific heats (here equal to 1.4), $\mathbf{d}(\mathbf{u}) = \frac{1}{2}\left(\nabla\mathbf{u} + \nabla\mathbf{u}^T\right)$ is the strain tensor, and $\tau(\mathbf{u}) = [2\mathbf{d}(\mathbf{u}) - \frac{2}{3}(\nabla\cdot\mathbf{u})\mathbf{I}]$ is the stress tensor per unit viscosity. Here, we assume that the viscosity and the thermal conductivity of the fluid are constant and independent of the temperature.

Equations (1) are made non-dimensional by using the cylinder diameter D as length scale and the upstream quantities U_∞, ρ_∞, T_∞; the dimensionless pressure is defined as $\frac{p-p_\infty}{p_\infty U_\infty^2}$. Thus, the Reynolds ($Re$) and Mach ($M$) numbers can be expressed as

$$Re = \frac{\rho_\infty U_\infty D}{\mu}, \qquad M = \frac{U_\infty}{\sqrt{\gamma R T_\infty}},$$

where R is the ideal gas constant.

B. Stability analysis

The instability of the flow is here investigated within the classical framework of linear theory and normal-mode analysis. The solution $[\boldsymbol{u}, p, T, \rho]$ is decomposed into a steady state $[\boldsymbol{U}_b, p_b, T_b, \rho_b](\boldsymbol{x})$ and a small unsteady perturbation field $[\boldsymbol{u}', p', T', \rho'](\boldsymbol{x}, t)$ as

$$\boldsymbol{u}(\boldsymbol{x}, t) = \boldsymbol{U}_b(\boldsymbol{x}) + \epsilon\boldsymbol{u}'(\boldsymbol{x}, t), \tag{2a}$$

$$p(\boldsymbol{x}, t) = p_b(\boldsymbol{x}) + \epsilon p'(\boldsymbol{x}, t), \tag{2b}$$

$$T(\boldsymbol{x}, t) = T_b(\boldsymbol{x}) + \epsilon T'(\boldsymbol{x}, t), \tag{2c}$$

$$\rho(\boldsymbol{x}, t) = \rho_b(\boldsymbol{x}) + \epsilon\rho'(\boldsymbol{x}, t), \tag{2d}$$

where the amplitude ϵ is assumed to be small. In order to investigate the long-term (asymptotic) stability of the cylinder wake, the evolution of the perturbation is here expressed by means of the classical normal mode form[14]

$$[\boldsymbol{u}', p', T', \rho'](\boldsymbol{x}, t) = \sum_n [\hat{\boldsymbol{u}}_n, \hat{p}_n, \hat{T}_n, \hat{\rho}_n](\boldsymbol{x})\ \exp\{\lambda_n t\} + c.c., \tag{3}$$

where $c.c.$ is the complex conjugate. The disturbances are then described by the complex eigenmodes $[\hat{\boldsymbol{u}}_n, \hat{p}_n, \hat{T}_n, \hat{\rho}_n]$ and the corresponding complex eigenvalues $\lambda_n = \sigma_n + i\omega_n$, where ω_n is the eigenfrequency and σ_n represents the growth rate. By introducing the flow decomposition (2) into the system (1), the two following problems are obtained:

(i) at order 0, the steady version of compressible Navier-Stokes equations determining the spatial structure of the base flow,

$$\mathbf{U}_b\cdot\nabla\rho_b + \rho_b\nabla\cdot\mathbf{U}_b = 0, \tag{4a}$$

$$\rho_b\mathbf{U}_b\cdot\nabla\mathbf{U}_b + \nabla P_b - \frac{1}{Re}\nabla\cdot\tau(\mathbf{U}_b) = \mathbf{0}, \tag{4b}$$

$$\rho_b\mathbf{U}_b\cdot\nabla T_b + (\gamma-1)\rho_b T_b\nabla\cdot\mathbf{U}_b - \gamma(\gamma-1)\frac{M^2}{Re}\tau(\mathbf{U}_b) : \mathbf{d}(\mathbf{U}_b) - \frac{\gamma}{Pr\,Re}\nabla^2 T_b = 0, \tag{4c}$$

$$\rho_b T_b - 1 - \gamma M^2 P_b = 0, \tag{4d}$$

(ii) at order 1, the generalized eigenvalue problem providing the eigenvalues and the corresponding eigenmodes

$$\lambda_n\hat{\rho}_n + \mathbf{U}_b\cdot\nabla\hat{\rho}_n + \hat{\mathbf{u}}_n\cdot\nabla\rho_b + \rho_b\nabla\cdot\hat{\mathbf{u}}_n + \hat{\rho}_n\nabla\cdot\mathbf{U}_b = 0, \quad (5a)$$

$$\lambda_n\rho_b\hat{\mathbf{u}}_n + \hat{\rho}_n\mathbf{U}_b\cdot\nabla\mathbf{U}_b + \rho_b\hat{\mathbf{u}}_n\cdot\nabla\mathbf{U}_b + \rho_b\mathbf{U}_b\cdot\nabla\hat{\mathbf{u}}_n + \nabla\hat{p}_n - \frac{1}{Re}\nabla\cdot\tau(\hat{\mathbf{u}}_n) = \mathbf{0}, \quad (5b)$$

$$\rho_b\hat{T}_n\lambda_n + \hat{\rho}_n\mathbf{U}_b\cdot\nabla T_b + \rho_b\hat{\mathbf{u}}_n\cdot\nabla T_b + \rho_b\mathbf{U}_b\cdot\nabla\hat{T}_n + (\gamma-1)\left(\hat{\rho}_n T_b\nabla\cdot\mathbf{U}_b + \rho_b\hat{T}_n\nabla\cdot\mathbf{U}_b + \rho_b T_b\nabla\cdot\hat{\mathbf{u}}_n\right) - \gamma(\gamma-1)\frac{M^2}{Re}\left[\tau(\hat{\mathbf{u}}_n):\mathbf{d}(\mathbf{U}_b) + \tau(\mathbf{U}_b):\mathbf{d}(\hat{\mathbf{u}}_n)\right] - \frac{\gamma}{Pr\,Re}\nabla^2\hat{T}_n = 0, \quad (5c)$$

$$\hat{\rho}_n T_b + \rho_b\hat{T}_n - \gamma M^2\hat{P}_n = 0. \quad (5d)$$

The base flow problem (4) is supplemented by no-slip boundary condition ($\mathbf{u} = \mathbf{0}$) and adiabatic temperature condition on the cylinder surface, free-stream flow conditions at the inlet ($\mathbf{u} = [1, 0]$, $\rho = 1$, $T = 1$), and natural outflow conditions at the outlet. The conditions for the stability problem are simply derived from the ones of the base flow. Finally, we recall that a negative growth rate, i.e., $\sigma_n < 0$, means linear stability, while a positive growth rate, i.e., $\sigma > 0$, means instability.

C. Stability of the mean flow

One of the main goals of computational fluid dynamics (CFD) is the prediction of the unsteady features of the flow like the spatial distribution of the unsteadiness or the inherent frequency that characterizes the nonlinear system. The linear stability analysis on the base flow performed far from the critical conditions is not able to provide such information because it is unable to take into account nonlinear effects.[15,16] In order to surmount this difficulty, Pier[16] and Mittal[17] performed a stability analysis around a *mean flow*. They found that the resulting frequency predicts well the frequency of the saturated limit cycles. Such an analysis, however, provides accurate results only in the case where the considered limit cycle is dominated by a single frequency: in other words, the resulting periodic solution should be almost monochromatic. However, Mantič-Lugo and Gallaire[18] used this approach to investigate also a selective noise amplifier, the backward facing step, that is characterized by large linear amplification to external perturbations in a particular frequency range.

Sipp and Lebedev[19] focused on self-excited systems that present a strong dominating frequency. Gudmundsson and Colonius[20] experimentally studied a turbulent jet flow. They investigated the extent to which pressure and velocity fluctuations in subsonic, turbulent round jets can be described as linear perturbations to the mean flow field. The authors used the parabolized stability equations (PSEs) around the measured jet mean flow field. They concluded that the evolution of the largest-scale structures of turbulent jets can be predicted by just considering perturbations to the mean flow field neglecting any non-zero frequency disturbance interactions.

Recently Mantič-Lugo *et al.*[12,21] proposed a self-consistent model for the saturation dynamics of the vortex shedding around the mean flow in the unstable cylinder wake. Their model provided an excellent prediction of the mean flow and the associated vortex street in terms of frequency, amplitude, and spatial structure. The obtained Reynolds stress divergence estimates very well the structure of the exact solution of the full DNS. We will apply this elegant theory in the present paper. We will describe accurately it in Sec. II D. Finally, we note that Beneddine *et al.*[22] provided theoretical conditions for the use and meaning of a stability analysis around a mean flow.

D. Self-consistent mean-flow model

In the present section, we briefly recall the self-consistent mean-flow model proposed in Ref. 12; we refer to this reference for further details. The starting point of this approach is the decomposition of the total flow state $\mathbf{q} = [\boldsymbol{u}, p, T, \rho]$ in a mean state $\overline{\mathbf{q}} = [\overline{\boldsymbol{u}}, \overline{p}, \overline{T}, \overline{\rho}]$ and an unsteady perturbation $\mathbf{q}' = [\boldsymbol{u}', p', T', \rho']$,

$$\mathbf{q} = \overline{\mathbf{q}} + \mathbf{q}', \quad (6)$$

where the time-average operator is defined as $\overline{\alpha} = \frac{1}{\tilde{T}}\int_0^{\tilde{T}}\alpha(t)\,dt$ and $\tilde{T}$ is the limit cycle period of the considered case. Injecting Eq. (6) in the compressible Navier-Stokes equations (1) and performing a time average on the resulting system, we get the following set of equations:

$$\overline{\mathbf{u}}\cdot\nabla\overline{\rho} + \overline{\rho}\nabla\cdot\overline{\mathbf{u}} = -\overline{\mathbf{u}'\cdot\nabla\rho'} - \overline{\rho'\nabla\cdot\mathbf{u}'}, \quad (7a)$$

$$\overline{\rho}\overline{\mathbf{u}}\cdot\nabla\overline{\mathbf{u}} + \nabla\overline{p} - \frac{1}{Re}\nabla\cdot\tau(\overline{\mathbf{u}}) = -\overline{\rho'\frac{\partial\mathbf{u}'}{\partial t}} - \overline{\rho'\overline{\mathbf{u}}\cdot\nabla\mathbf{u}'} - \overline{\overline{\rho}\mathbf{u}'\cdot\nabla\mathbf{u}'} - \overline{\rho'\mathbf{u}'\cdot\nabla\overline{\mathbf{u}}} - \overline{\rho'\mathbf{u}'\cdot\nabla\mathbf{u}'}, \quad (7b)$$

$$\overline{\rho}\overline{\mathbf{u}}\cdot\nabla\overline{T} + (\gamma-1)\overline{\rho}\overline{T}\nabla\cdot\overline{\mathbf{u}} - \gamma(\gamma-1)\frac{M^2}{Re}\tau(\overline{\mathbf{u}}):\mathbf{d}(\overline{\mathbf{u}}) - \frac{\gamma}{Pr\,Re}\nabla^2\overline{T} = -\overline{\rho'\frac{\partial T'}{\partial t}} - \overline{\overline{\rho}\mathbf{u}'\cdot\nabla T'} - \overline{\rho'\overline{\mathbf{u}}\cdot\nabla T'} - \overline{\rho'\mathbf{u}'\cdot\nabla\overline{T}} - \overline{\rho'\mathbf{u}'\cdot\nabla T'} - \overline{\overline{\rho}T'\nabla\cdot\mathbf{u}'} - (\gamma-1)\left[\overline{\rho'\overline{T}\nabla\cdot\mathbf{u}'} + \overline{\rho'T'\nabla\cdot\overline{\mathbf{u}}} + \overline{\rho'T'\nabla\cdot\mathbf{u}'}\right] + \gamma(\gamma-1)\frac{M^2}{Re}\overline{\tau(\mathbf{u}'):\mathbf{d}(\mathbf{u}')}, \quad (7c)$$

$$\overline{\rho}\overline{T} - 1 - \gamma M^2\overline{P} = -\overline{\rho'T'}. \quad (7d)$$

Following Ref. 12, we can write the equation that governs the unsteady perturbation $\mathbf{q}'$ as

$$\frac{\partial \mathbf{q}'}{\partial t} + \mathbf{L}(\overline{\mathbf{q}}, \mathbf{q}') = -\mathbf{F}(\mathbf{q}'), \tag{8}$$

where $\mathbf{F}$ represents the interactions between the different harmonics. In this work, we neglect this nonlinear term and the perturbations are sought in the normal mode form

$$\mathbf{q}'(\mathbf{x}, t) = \tilde{\mathbf{q}} \exp[\eta t] + \tilde{\mathbf{q}}^* \exp[\eta^* t], \tag{9}$$

and therefore Eq. (8) reduces to a linear stability analysis around the state $\overline{\mathbf{q}}$. Moreover, as a consequence of Eq. (9), the system of Eqs. (7) can be rewritten as

$$\overline{\mathbf{u}} \cdot \nabla \overline{\rho} + \overline{\rho} \nabla \cdot \overline{\mathbf{u}} = -2A^2 \left[\Re\{\tilde{\tilde{\mathbf{u}}}^* \cdot \nabla \tilde{\rho}\} + \Re\{\rho^* \nabla \cdot \tilde{\mathbf{u}}\} \right], \tag{10a}$$

$$\overline{\rho}\overline{\mathbf{u}} \cdot \nabla \overline{\mathbf{u}} + \nabla \overline{p} - \frac{1}{Re} \nabla \cdot \tau(\overline{\mathbf{u}}) = -2A^2 \left[\Re\{\tilde{\rho}^* i\eta_i \tilde{\mathbf{u}}\} + \Re\{\tilde{\rho}^* \tilde{\mathbf{u}} \cdot \nabla \overline{\mathbf{u}}\} + \Re\{\tilde{\rho}^* \overline{\mathbf{u}} \cdot \nabla \tilde{\mathbf{u}}\} + \Re\{\overline{\rho} \tilde{\mathbf{u}}^* \cdot \nabla \tilde{\mathbf{u}}\} \right], \tag{10b}$$

$$\begin{aligned} &\overline{\rho}\overline{\mathbf{u}} \cdot \nabla \overline{T} + (\gamma - 1)\overline{\rho}\overline{T} \nabla \cdot \overline{\mathbf{u}} - \gamma(\gamma - 1)\frac{M^2}{Re} \tau(\overline{\mathbf{u}}) : \mathbf{d}(\overline{\mathbf{u}}) - \frac{\gamma}{Pr\, Re} \nabla^2 \overline{T} \\ &= -2A^2 \left[\Re\{\overline{\rho}\tilde{\mathbf{u}} \cdot \nabla \tilde{T}\} + \Re\{\tilde{\rho}^* \overline{\mathbf{u}} \cdot \nabla \tilde{T}\} + \Re\{\tilde{\rho}^* \tilde{\mathbf{u}} \cdot \nabla \overline{T}\} \right] + -2A^2(\gamma - 1) \left[\Re\{\overline{\rho} \tilde{T}^* \nabla \cdot \tilde{\mathbf{u}}\} + \Re\{\tilde{\rho}^* \tilde{T} \nabla \cdot \overline{\mathbf{u}}\} \right. \\ &\quad \left. + \Re\{\tilde{\rho}^* \overline{T} \nabla \cdot \tilde{\mathbf{u}}\} \right] + -2A^2 \left[\Re\{\tilde{\rho}^* i\eta_i \tilde{T}\} - \gamma(\gamma - 1)\frac{M^2}{Re} \Re\{\tau(\tilde{\mathbf{u}})^* : \mathbf{d}(\tilde{\mathbf{u}})\} \right], \end{aligned} \tag{10c}$$

$$\overline{\rho}\overline{T} - 1 - \gamma M^2 \overline{P} = -2A^2 \Re\left\{\tilde{\rho}^* \tilde{T}\right\}, \tag{10d}$$

where $\Re\{\}$ is the real-part operator and A is the amplitude of the perturbation. Here the perturbation is normalized by the L^2 inner product computed on the computational domain, namely, $(a, b) = b^H B a$, where B is the mass matrix of the stability problem. Thus the amplitude of the fluctuation is defined as $A = \int_\Omega \langle \overline{\rho} u'^2 + \overline{\rho} T'^2 + \rho'^2 \rangle d\Omega$. Note that when the Mach number is approaching the incompressible case limit, the temperature T' and density ρ' fluctuations become negligible, leading to the same amplitude definition used by Mantič-Lugo *et al.*[12] The mean flow and the shedding fluctuations with their amplitude are retrieved by solving Eqs. (10) together with the stability equations around the forced base state and by imposing that the perturbation is marginally stable.

III. NUMERICAL METHOD

A finite-element method is used to solve the problems involved in the present paper. The unknown $[u, v, p, T, \rho]$ is spatially discretized on an unstructured mesh obtained by a Delaunay triangulation procedure. In particular, we used the built-in mesh generator (Bamg) implemented in Freefem++ (http://www.freefem.org). We adopted P2 elements for the velocity components and P1 elements for the pressure, temperature, and density fields. The discretization of the systems has been performed by using the Freefem++ libraries. The nonlinear system of algebraic equations, deriving from the discretization of the nonlinear equations along with their boundary conditions, is solved by a Newton–Raphson procedure.

TABLE I. Compressible flow past a circular cylinder. We performed several tests to check the influence of the mesh parameters on the accuracy of the results. Here x_{in} and x_{out} are the locations of the inlet and the outlet, while y_{ext} is the location of the lateral boundaries of the computational domain. We built 4 different mesh groups: (M_1)–(M_2)–(M_3, M_4, M_5)–(M_6, M_7, M_8). The last two groups (M_3, M_4, M_5)–(M_6, M_7, M_8) have, respectively, the same spatial extent but with different mesh refinement. Finally, $n_{tr.}$ is the total number of triangles inside the computational domain.

	M_1	M_2	M_3	M_4	M_5	M_6	M_7	M_8
x_1	−5	−5	−5	−5	−5	−7	−7	−7
x_2	17	25	25	25	25	30	30	30
x_3	−15	−20	−25	−25	−25	−30	−30	−30
x_4	40	65	80	80	80	100	100	100
x_{in}	−150	−250	−300	−300	−300	−350	−350	−350
x_{out}	250	350	500	500	500	600	600	600
y_1	2.5	3	3	3	3	3.5	3.5	3.5
y_2	10	15	18	18	18	20	20	20
y_{ext}	175	250	300	300	300	350	350	350
$n_{tr.}$	132 498	143 165	162 089	305 643	606 323	203 024	423 762	921 018

TABLE II. Convergence test on the leading eigenvalue at $Re = 150$.

Mesh	Eigenvalue ($\sigma + \mathbf{i}\omega$)
M_1	+0.151 096 ± **i**0.645 211
M_2	+0.152 003 ± **i**0.645 379
M_3	+0.152 811 ± **i**0.645 388
M_4	+0.152 983 ± **i**0.645 403
M_5	+0.152 991 ± **i**0.645 409
M_6	+0.152 977 ± **i**0.645 397
M_7	+0.152 984 ± **i**0.645 402
M_8	+0.152 994 ± **i**0.645 408

At each step of this method, we solve the arising linear systems by the multifrontal, sparse LU solver MUMPS (Ref. 23).

Figure 1 shows the mesh structure that we used for our simulations. We can distinguish 3 different regions: (i) an inner region (dark gray), near the cylinder surface, (ii) a middle region, and (iii) an outer region (white) far from the bluff body. In this last region, we introduced a sponge zone to damp the acoustic waves and avoid reflections. We follow the approach proposed by Rowley *et al.*[24] which consists in adding a forcing term on the right-hand side of the governing equations. In particular, we introduced the term $-\tilde{\beta}(x,y)(\mathbf{q}-\mathbf{q}_{fs})$, where $\mathbf{q}_{fs}$ is the free-stream field imposed at the inlet. The damping function $\tilde{\beta}(x,y)$ must be a decaying function as proposed by Rowley *et al.*[24] Here, we use the same function adopted by Yamouni *et al.*,[25]

$$\tilde{\beta}(x,y) = 0, \quad if \quad x_3 \le x \le x_4 \quad and \quad |y| \le y_2, \tag{11a}$$

$$\tilde{\beta}(x,y) = \left|1 - \frac{1}{M}\right| f(x_3, x), \quad if \quad x < x_3 \quad and \quad |y| \le y_2, \tag{11b}$$

$$\tilde{\beta}(x,y) = \left|1 + \frac{1}{M}\right| f(x, x_4), \quad if \quad x > x_4 \quad and \quad |y| \le y_2, \tag{11c}$$

$$\tilde{\beta}(x,y) = \tilde{\beta}(x, y_2) + \left|\frac{1}{M}\right| f(y, y_4), \quad if \quad |y| > y_2, \tag{11d}$$

with

$$f(a,b) = \frac{2\alpha}{l_s^2}(a-b),$$

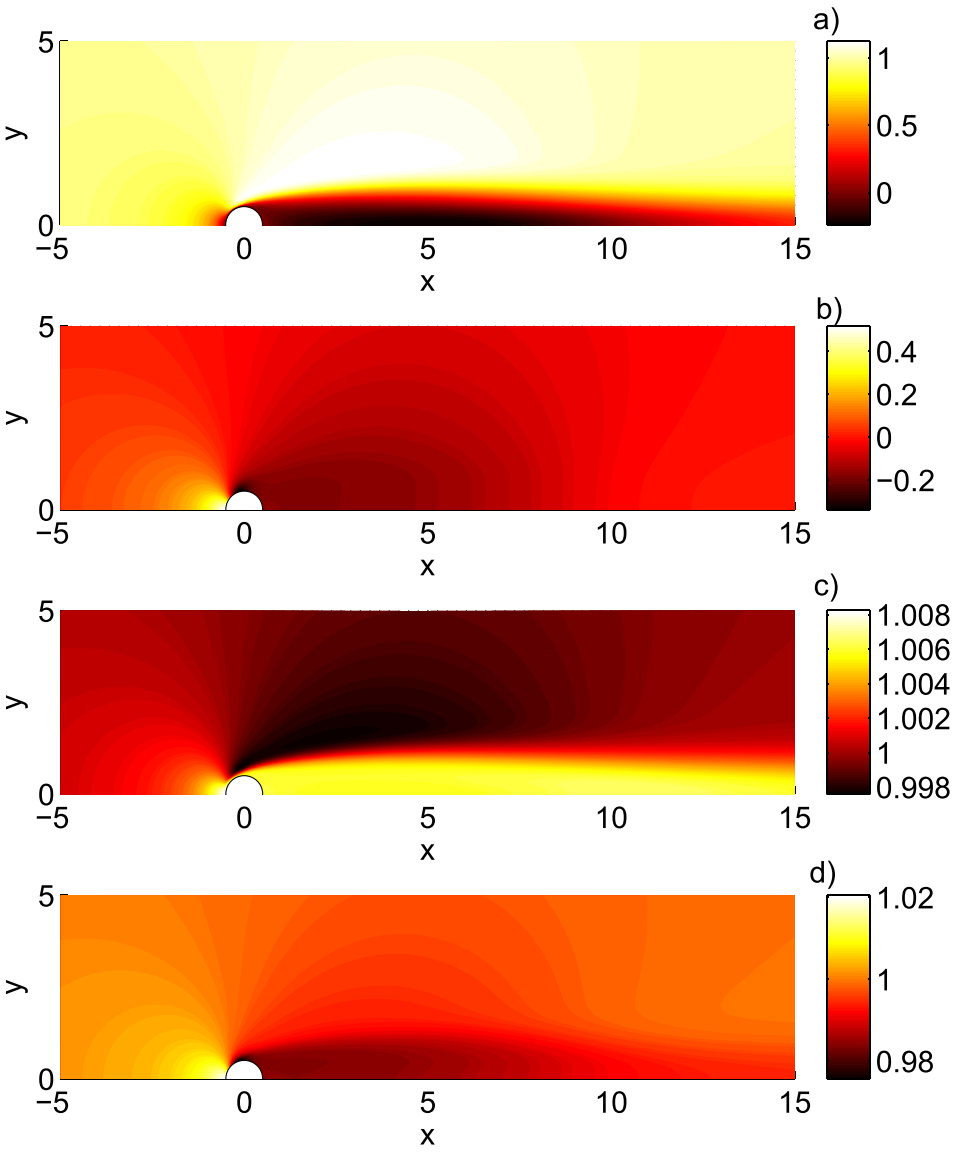

FIG. 2. Base flow: contour plots of (a) streamwise velocity U_b, (b) pressure field p_b, (c) temperature T_b, and (d) density ρ_b. Parameter settings: $M = 0.2$, $Re = 150$.

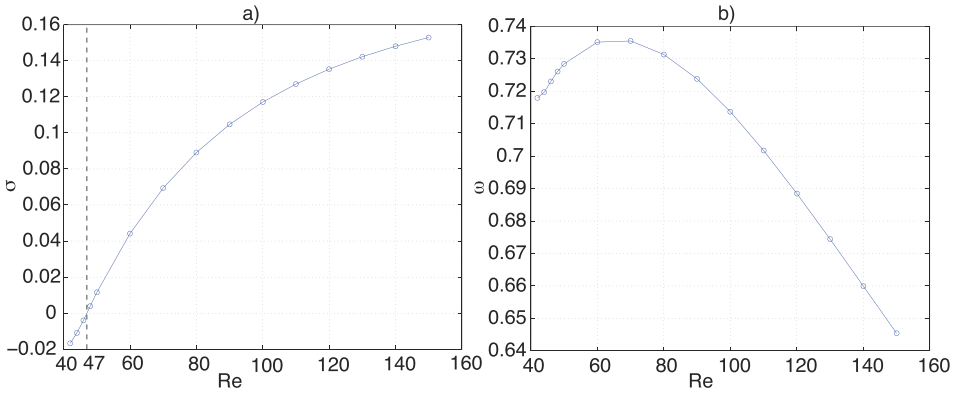

FIG. 3. Linear stability results at $M = 0.2$: (a) growth rate σ and (b) eigenfrequency ω as a function of the Reynolds number.

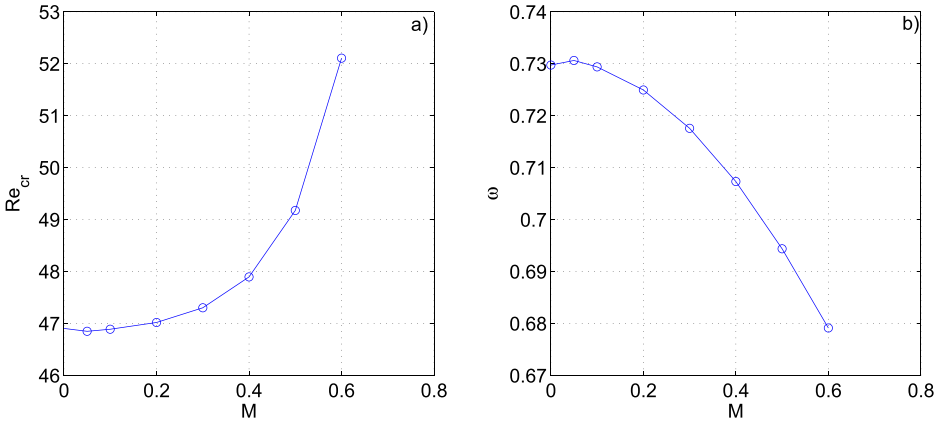

FIG. 4. (a) Critical Reynolds number and (b) critical eigenfrequency ω as a function of the Mach number.

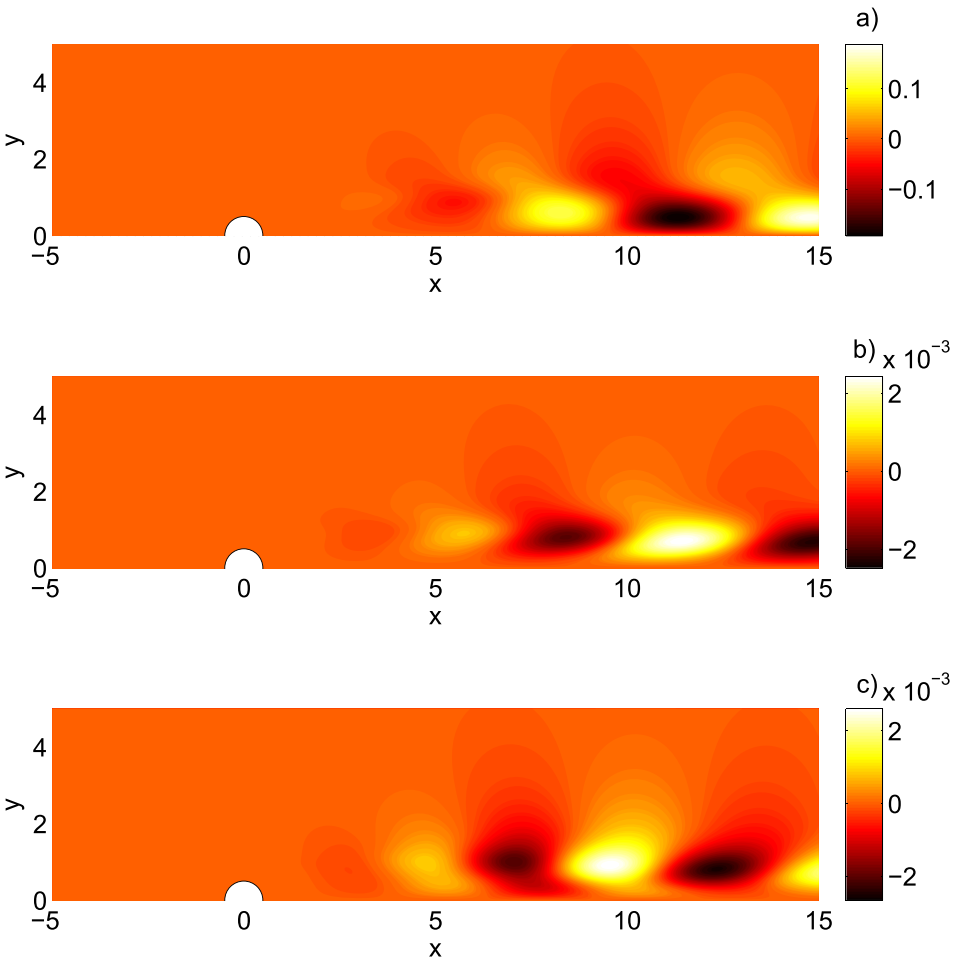

FIG. 5. Direct global mode. Contour plot of (a) $\Re\{\hat{u}\}$, (b) $\Re\{\hat{\rho}\}$, and (c) $\Re\{\hat{T}\}$. Parameter settings: $M = 0.2$, $Re = 150$.

where α is a parameter related to the attenuation rate of the propagating wave. We performed several tests to properly choose the size of the domain and of the value of the parameter α. For the computations presented in this paper, we selected $2\alpha/l_s^2 = 10^{-4}$.

We used different meshes to test the influence of the different parameters on the accuracy of our results. Table I shows the characteristics of these grids and the total number of triangles inside the computational domain. The convergence test (see Table II) on the leading eigenvalue at $Re = 150$ clearly shows that the mesh M_4 provides accurate results.

A. Self-consistent model solution

In the work of Mantič-Lugo *et al.*,[12] the nonlinear system of equations of the self-consistent model is solved iteratively by means of a nested iteration loop. In the inner loop, they fix the amplitude A and they solve sequentially the forced base-state equations and the stability analysis around the mean flow until convergence. In the outer loop, the amplitude is varied until the perturbation becomes marginally stable.

In the current work, we used a monolithic approach. The fully coupled system of equations (forced base state, linear stability, perturbation normalization, and a phase constraint) is solved by using a Newton-Raphson method where the Jacobian is analytically determined and the unknowns are $[\overline{\mathbf{q}}, \Re(\tilde{\mathbf{q}}), \Im(\tilde{\mathbf{q}}), \mathbf{A}, \omega]$. Note that we split the perturbation into its real and imaginary parts and in the stability problem the growth rate is assumed to be null. The equations for the amplitude and the frequency are, respectively, the mode normalization and a condition on the value of the perturbation phase. At each step, the arising linear system is solved by the multifrontal, sparse LU solver MUMPS. Compared to the segregated procedure, here we have an increased computational cost but on the other hand we do not have the convergence problem described by Mantič-Lugo *et al.*[21] as the Reynolds number increases. The procedure converged in the considered range of Reynolds and Mach numbers in about 5 iterations, given a reasonable initial guess, which is typically a previous self-consistent solution.

IV. RESULTS

A. Base flow and global modes

We focus our attention on the stability characteristics of the base flow, i.e., the solution of the steady form of the compressible Navier-Stokes equations (1). We show the typical

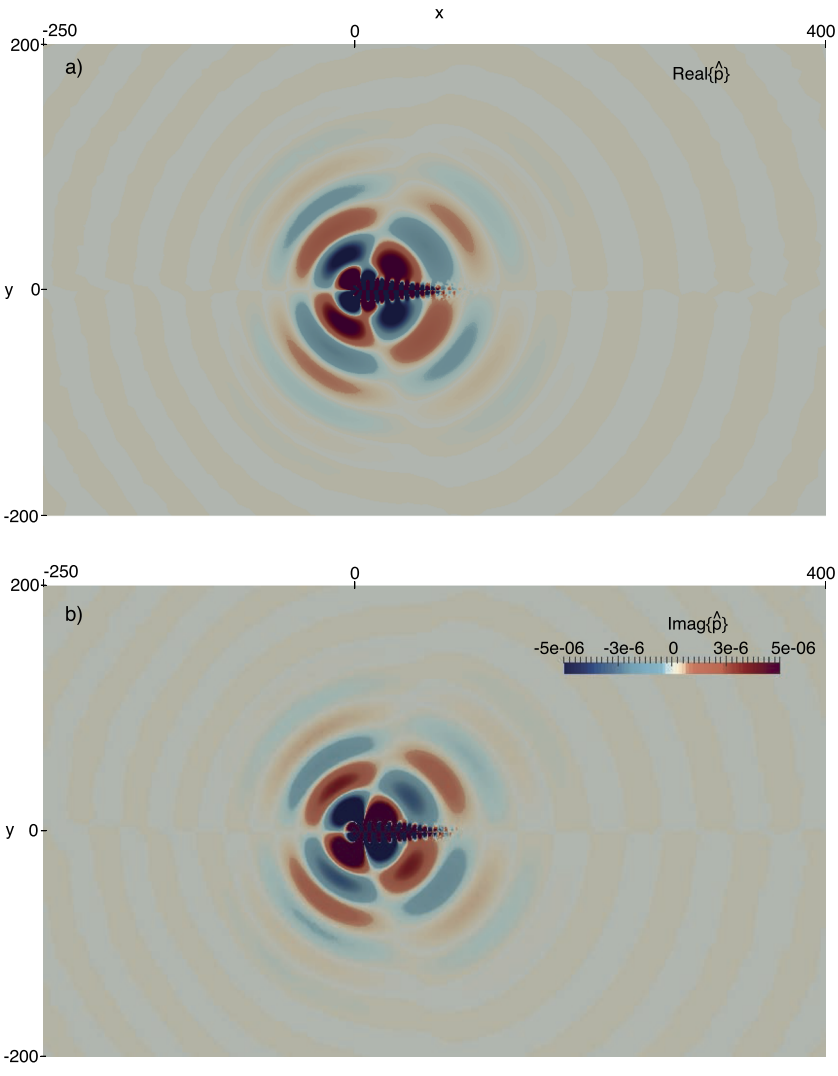

FIG. 6. (a) Real and (b) imaginary parts of the global $\hat{p}$ mode.

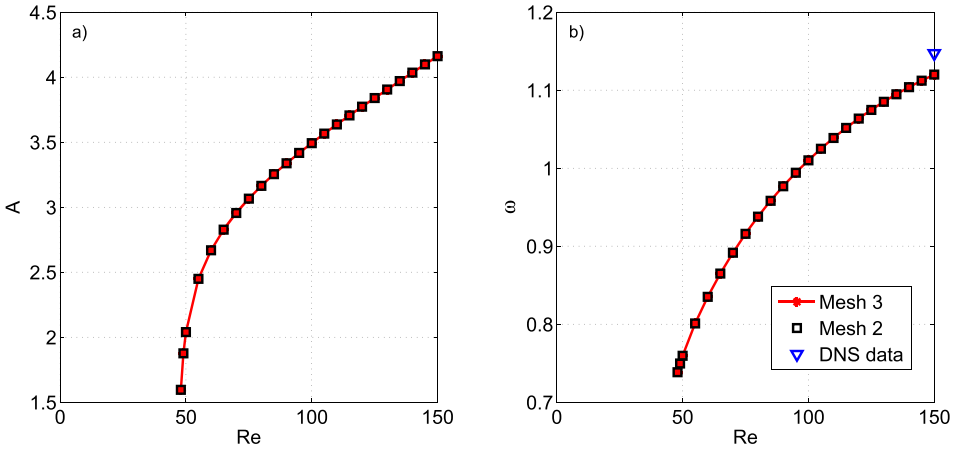

FIG. 7. Self-consistent model results. We depict (a) the amplitude A and (b) the frequency ω as a function of the Reynolds number for a Mach number equal to 0.2. We report also the DNS frequency extracted from Inoue and Hatakeyama's[13] data (see, e.g., Fig. 9).

shape of the base flow through contours of (a) streamwise velocity U_b, (b) pressure p_b, (c) temperature T_b, and (d) density ρ_b in Fig. 2. In particular, we focus our attention on the most unstable eigenvalue provided by eigenproblem (5). We show the evolution of the real part of the leading eigenvalue in Fig. 3(a), while Fig. 3(b) shows the imaginary part of the eigenvalue, i.e., the linear frequency of the global mode. The critical Reynolds number is then identified by checking where the real part of the leading eigenvalue changes its sign. We found that the onset of the instability is $Re_{cr} \approx 47$ which is very similar to the threshold reported in the incompressible case $Re_{cr} \approx 46.7$ (see the work of Giannetti and Luchini[26] for the numerical prediction or the work of Williamson[1] for the experimental results). Figure 4 shows the critical Reynolds number and the associated frequency as a function of the Mach number. We found that the onset of the instability occurs at a larger Reynolds number as the Mach number increases, while the eigenfrequency at the critical condition becomes smaller.

We chose to adopt a Mach number $M = 0.2$ and a Reynolds number $Re = 150$ to be consistent with the parameters adopted in the mean-flow stability analysis. In this way, we can easily compare the results provided by these two different approaches.

We depict the spatial structure of the direct global mode in Fig. 5. In particular, Fig. 5(a) shows the distribution of the real part of the streamwise velocity component $\Re\{\hat{u}\}$ of the leading eigenmode at $Re = 150$ and $M = 0.2$. We note that the spatial features of the global mode weakly change in the range of Reynolds numbers reported in Fig. 3 (not shown here for the sake of brevity). Generally, as for the incompressible case, the maximum value of the streamwise fluctuations moves upstream when the Reynolds number is increased. The density $\Re\{\hat{\rho}\}$ and the temperature $\Re\{\hat{T}\}$ components of the global mode are dominated by streamwise fluctuations located downstream of the circular cylinder. Both these fields are antisymmetric with respect to the x-axis.

Figure 6 depicts separately the real (a) and imaginary (b) part of the global pressure $\hat{p}$ mode. The development of the fluctuation pressure field shown in these figures clearly indicates that the pressure waves are generated from both the upper and lower sides of the cylinder in response to the vortex shedding. The same behaviour was found in the work of Inoue and Hatakeyama[13] by using direct numerical simulations.

B. Self-consistent model results: Sound propagation, frequency, and noise intensity

Mantič-Lugo *et al.*[12] proposed the self-consistent model summarized in Sec. II D which consists of a semi-linear coupling where the perturbation equation is linearized, while the quadratic Reynolds stresses are kept in the mean flow equation. They suggested adopting a monochromatic approximation of the limit cycle for the flow past a circular cylinder.

They managed to select the correct amplitude A of the linear perturbation on the mean flow solution. We recall here that the closure condition of the self-consistent model is the marginal stability condition, i.e., the amplitude is selected in order to have marginal stability of the perturbation field on the mean flow. In the present paper, we follow their procedure to

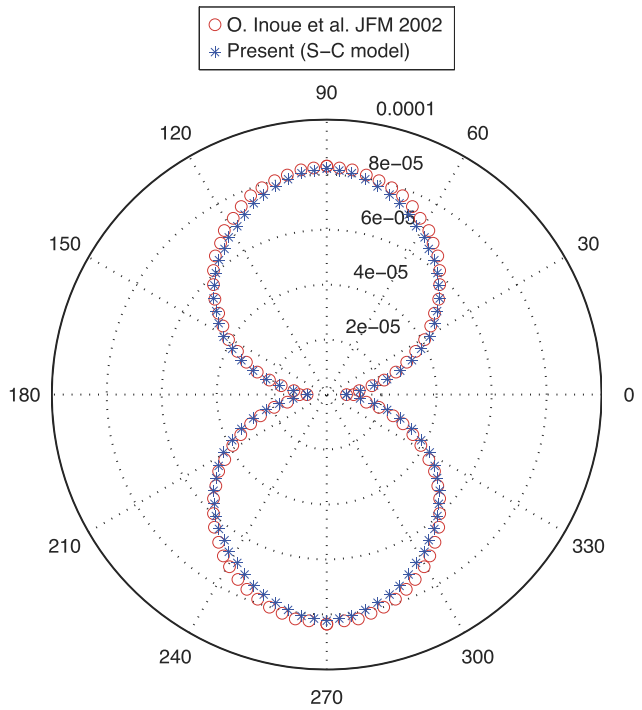

FIG. 8. Comparison on the directivity for the compressible flow past a circular cylinder. Polar plot of the root mean square of the fluctuation pressure $\Delta\tilde{p}^M$ (see the work of Inoue and Hatakeyama[13] for further details). Parameter settings: $M = 0.2$, $Re = 150$.

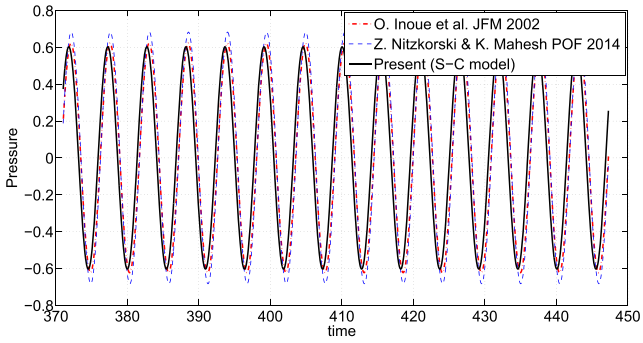

FIG. 9. Comparison on the time histories of the surface noise (Pa). For the Re = 150 cylinder, a comparison of the time histories of the surface noise is plotted versus those of Inoue and Hatakeyama[13] and Nitzkorski and Mahesh.[27] Parameter settings: $Re = 150$, $M = 0.2$, $\theta = \pi/2$, $r = 100D$.

correctly describe the acoustic field generated by the flow past the bluff body.

Figure 7 shows the dependence of the amplitude A and the related frequency on the Reynolds number for the fixed Mach number $M = 0.2$. We note that the DNS frequency extracted from the work of Inoue and Hatakeyama[13] compares well with the frequency computed by using the self-consistent model. On the other hand, the eigenfrequency provided by the standard linear stability analysis cannot predict the DNS frequency. We chose this particular Mach number because Inoue and Hatakeyama[13] and Nitzkorski and Mahesh[27] reported several numerical results for the same flow configuration considered in the present paper. Thus we will compare our results with the DNS data[13] and Ffowcs-Williams and Hawkings acoustic data.[27] In particular, Nitzkorski and Mahesh[27] proposed a dynamic end cap methodology to account for spurious contributions to the far-field sound within the context of the Ffowcs-Williams and Hawkings acoustic analogy. They correlated the quadrupole source terms over multiple planes to obtain a convection velocity that is then used to determine a corrective convective flux at the Ffowcs-Williams porous surface.

The amplitude curve [Fig. 7(a)] and the frequency curve closely resemble the curves reported in the work of Mantič-Lugo *et al.*[12] for the incompressible case. As in the case discussed by these authors, we found an excellent

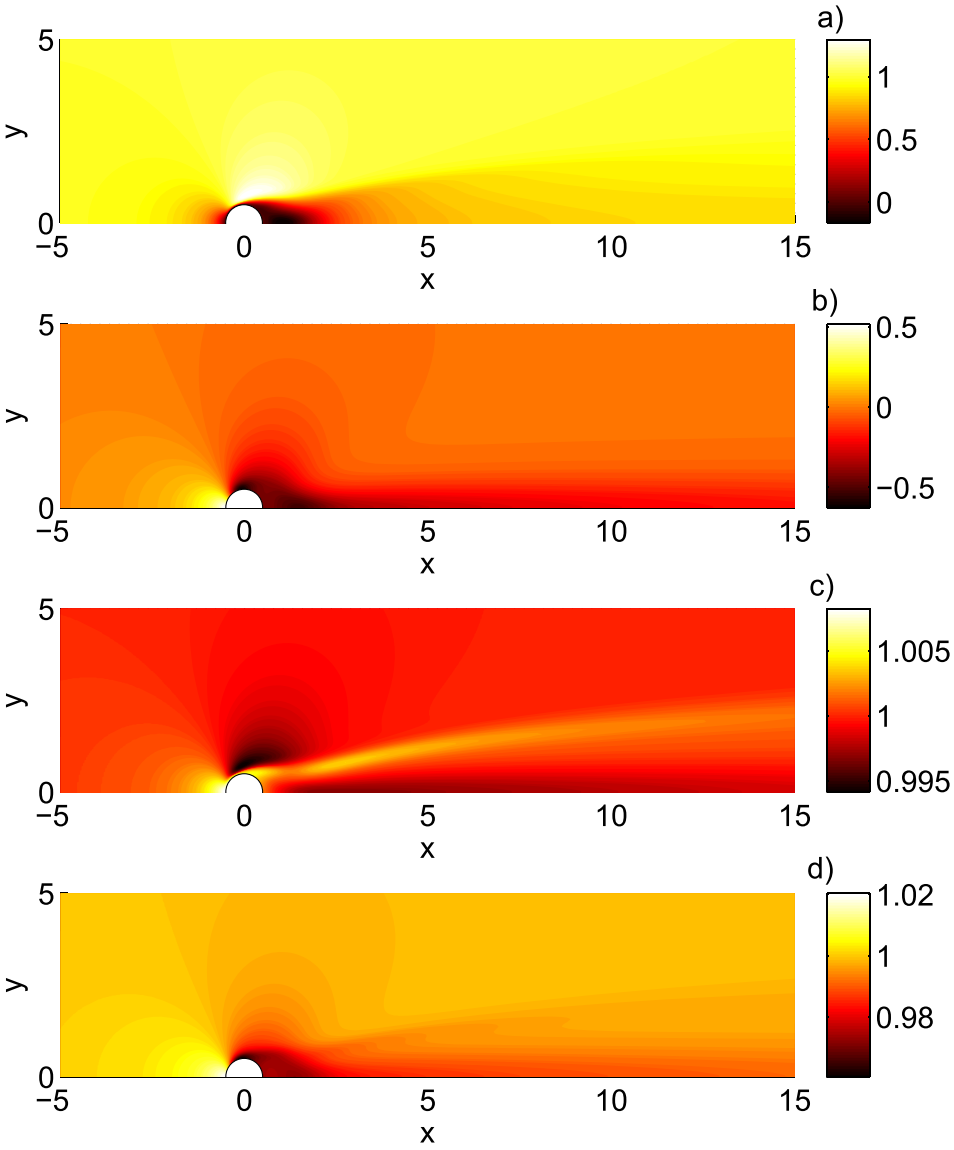

FIG. 10. Spatial structure of the mean flow field at $M = 0.2$ and $Re = 150$: (a) streamwise velocity, (b) pressure field, (c) temperature, and (d) density.

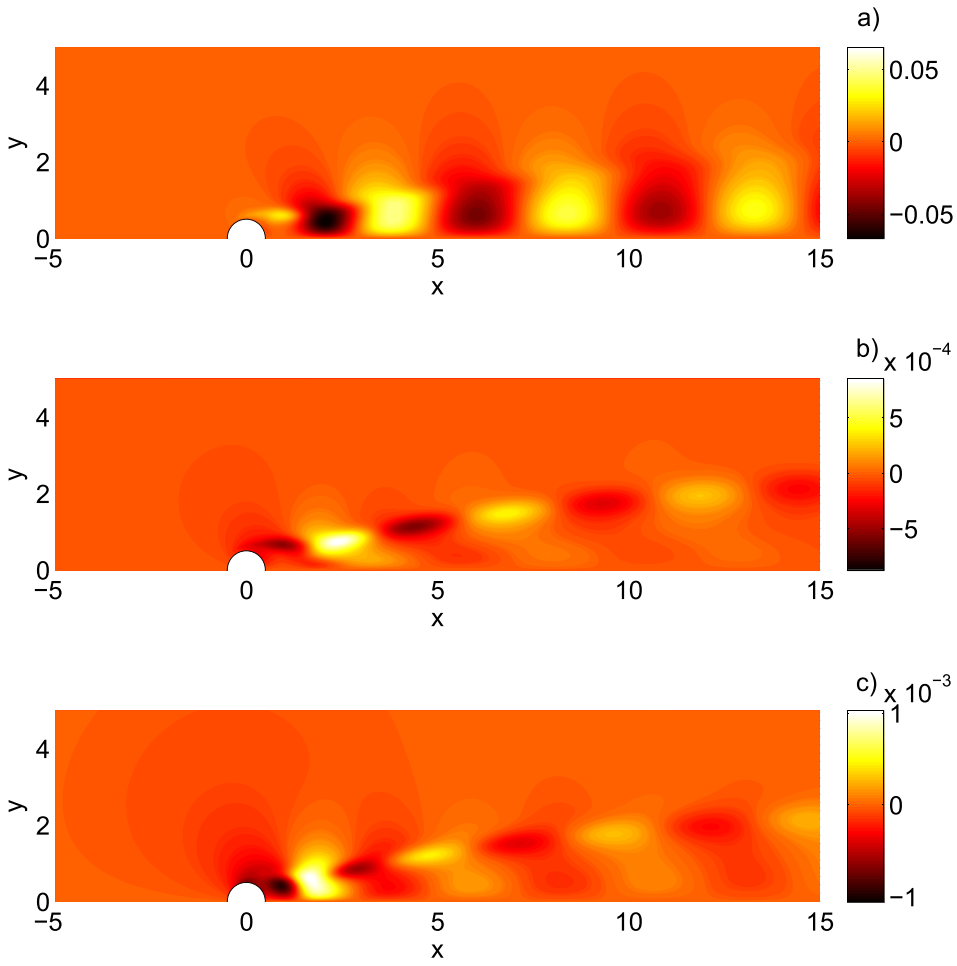

FIG. 11. Leading mode computed on the mean flow field depicted in Fig. 10: (a) real part of streamwise velocity perturbation, (b) real part of density perturbation, and (c) real part of the temperature.

approximation of the mean flow field and the perturbation on it. Figure 8 depicts the polar plot of the root mean square of the fluctuation pressures obtained by the self-consistent data. We found a very good agreement with the DNS results (see also Fig. 9) reported by Inoue and Hatakeyama.[13] This polar diagram shows the directivity of the pressure waves generated by the vortex shedding at the Reynolds number of 150. This plot confirms the dipolar nature of the sound field produced by the body. More importantly, we got the same directivity of Inoue and Hatakeyama[13] that is equal to $\theta \approx \pm 90°$. The results reported here are obtained taking into account the Doppler effect as discussed by Inoue and Hatakeyama.[13] The details of this procedure can be found in the Appendix.

The time histories of the pressure at $\theta = \pi/2$ and $r = 100D$ are compared (see Fig. 9) against those of Inoue and Hatakeyama[13] and Nitzkorski and Mahesh.[27] We found a very good agreement both on the amplitude of the wave and on its frequency. We underline that the quality of these results is strongly related to the excellent description of the mean flow and perturbation field provided by the self-consistent model. Thus, the application of it can be used to correctly capture both hydrodynamic and acoustic fields.

Figure 10 shows the velocity (a), pressure (b), temperature (c), and the density (d) mean flow fields. The velocity field is characterized by a shorter recirculation bubble than the base flow computed at the same Reynolds number. Significant differences with respect to the base flow can be observed also in the other fields of the mean flow.

The marginally stable mode computed on the mean flow field is shown in Fig. 11. As for the mean flow, the spatial structure of this mode is largely different from the global mode depicted in Fig. 5. In particular, the fluctuations are localized in different positions of the wake region. However, this "mean flow" mode presents the same symmetries of the global mode. As we did previously for the mode computed on the base flow field, we focus our attention to the pressure field because we are mainly interested in the mechanism of noise generation.

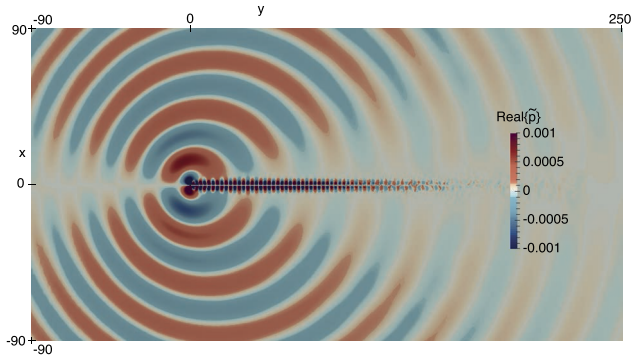

FIG. 12. Real part of the pressure mode computed on the mean flow. Parameters: $Re = 150$ and $M = 0.2$.

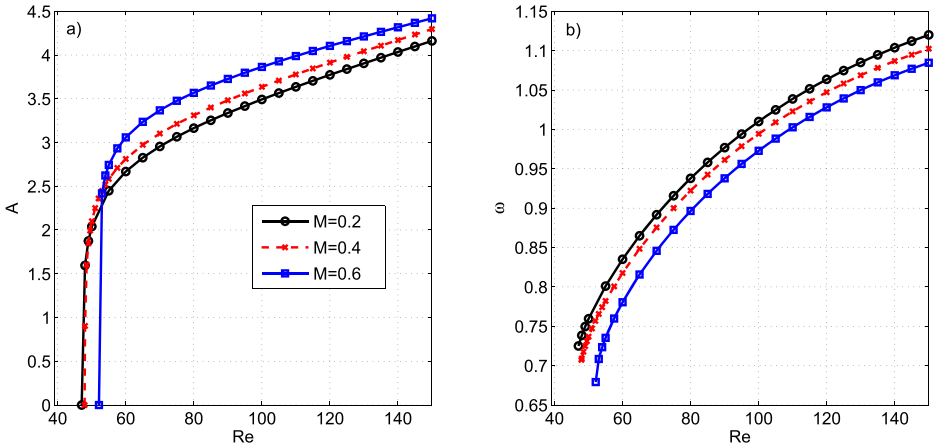

FIG. 13. Self-consistent model results for various Mach numbers. (a) Amplitude A and (b) the frequency ω as a function of the Reynolds number for the Mach number from 0.2 to 0.6.

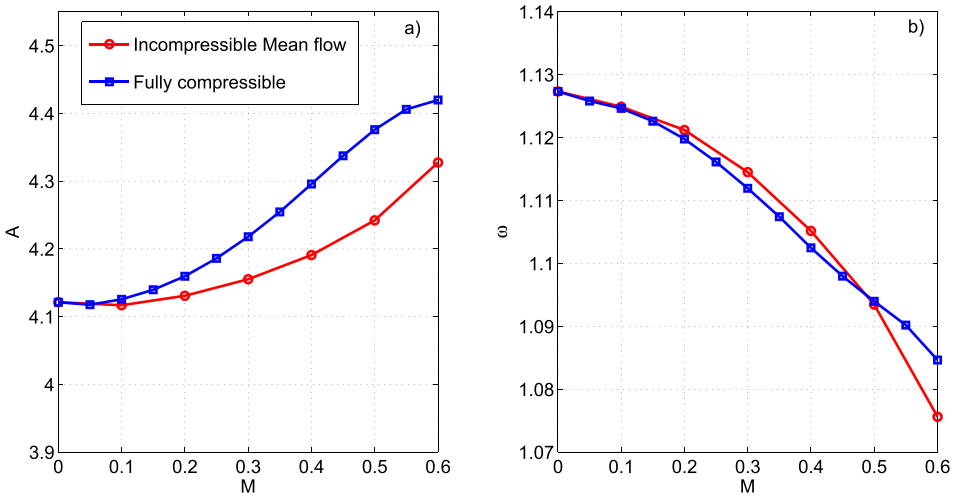

FIG. 14. Self-consistent model results. We depict (a) the amplitude A and (b) the frequency ω as a function of the Mach number for a Reynolds number equal to 150. We compare a fully compressible self-consistent model (red circle symbol) and one where only the perturbation part is compressible (blue square symbol).

Figure 12 shows the real $\Re\{\tilde{p}\}$ part of the pressure mode. As for the other components, the structure of this field is quite different with respect to the global mode. More importantly, we underline the excellent agreement between the present field and the one depicted by Inoue and Hatakeyama[13] in Fig. 15 of their work.

C. Effect of the Mach number

We investigate the effect of the Mach number on the results of the self-consistent model. Figure 13 shows the amplitude A and the frequency ω as a function of the Reynolds number for three different values of the Mach number, viz., (0.2, 0.4, 0.6). We observed that as the Mach number increases the frequency of the shedding reduces while the amplitude becomes larger. The effect is more accentuate at $M = 0.6$, where it is observable also the shift of the instability onset to $Re_{cr} \approx 53$.

We now investigate the effect of the compressibility of the mean flow on the results. In order to do that we used a self-consistent model where we set $M = 0$ only at the base flow level and we used the incompressible definition of amplitude A. Figure 14 shows that there is a small effect on both the amplitude and the shedding frequency (and therefore on the emitted-sound characteristics). The relative error for the amplitude and for the frequency is always lower than 3% and 0.8%, respectively, and increases only when M reaches larger values.

V. CONCLUSION

We numerically studied the sound generation produced by a circular cylinder in a uniform compressible flow.

The main idea of the present paper is to apply the new self-consistent model proposed by Mantič-Lugo *et al.*[12] to recover the intensity of the sound produced by the circular cylinder. This model is based on a monochromatic approximation of the limit cycle and allowed us to compute the amplitude of the resulting linear mode and the effects of saturation on the mode structure and acoustic field. This approach works well for the present configuration because the second harmonic does not contribute significantly to the limit cycle saturation for this flow.[12] However, should this assumption not be satisfied for different flow configurations, a new approach recently proposed by Meliga[28] to account also for the contribution of other harmonics could be exploited to extend the present analysis to more general problems.

For the test case, we chose to adopt a Mach number of 0.2 to compare our approach to the results available in the literature. For such a low Mach number, the classical linear stability analysis showed that the eigenvalues and the eigenmodes of the compressible flow are not very far from those of the incompressible flow. In particular, we found that the critical Reynolds number at $M = 0.2$ is $Re_{cr} \approx 47$, i.e., very similar to the incompressible one. This fact confirms the idea that the mean flow could be computed with an incompressible model

for such a low Mach number, thus reducing the computational burden.

Our results showed excellent agreement with those obtained by a fully compressible, direct numerical simulation (DNS)[13] and those derived by the application of the Ffowcs-Williams and Hawkings theory.[27] Finally, we found that the Mach number weakly affects the accuracy of the results.

APPENDIX: DOPPLER EFFECT

In this section, we briefly describe the procedure adopted by Inoue and Hatakeyama[13] to remove the Doppler effect from the polar diagrams. We refer to their paper for further details.

The procedure starts by defining the fluctuation pressure $\Delta\tilde{p}$ as $\Delta\tilde{p}(\mathbf{x},t) = \bar{p}(\mathbf{x},t) - \bar{p}_{mean}(\mathbf{x})$, where $\bar{p}$ is the flow pressure ($\bar{p} = p - p_\infty$) and $\bar{p}_{mean}$ is the time-averaged pressure. The (periodic) fluctuation pressure can be expressed by means of a Fourier series,

$$\Delta\tilde{p} = \sum_{n=0}^{\infty} A_n \cos(n\theta) + B_n \sin(n\theta).$$

The first term of this expansion is called the monopole A_0, the second term ($n = 1$) is called the dipole, and the third term ($n = 2$) is called the quadrupole. In the compressible flow past a circular cylinder, the sound generation is dominated by the dipole coefficient B_1. The Doppler effect modifies the inherent polar diagram as the Mach number increases. Thus, it is possible to introduce a modified fluctuation pressure $\Delta\tilde{p}^M$ as follows:

$$\Delta\tilde{p} = \sum_{n=0}^{\infty} \Delta\tilde{p}_n^M \left(\frac{r'}{r}\right)^n,$$

$$r' = r/(1 - M\cos\theta),$$

where the Doppler factor $(1 - M\cos\theta)$ is introduced. Thanks to this transformation, we are able to remove the Doppler effect from the flow field. In particular, we used this transformation to plot the polar diagram in Fig. 8.

[1] C. H. K. Williamson, "Vortex dynamics in the cylinder wake," Annu. Rev. Fluid Mech. **28**, 477–539 (1996).
[2] V. Strouhal, "Ueber eine besondere Art der Tonerregung," Ann. Phys. Chem. **241**, 216–251 (1878).
[3] J. H. Gerrard, "Measurements of the sound from circular cylinders in an air stream," Proc. Phys. Soc. Sect. B **68**, 453–461 (1955).
[4] M. J. Lighthill, "On sound generated aerodynamically: I. General theory," Proc. R. Soc. A **221**, 564–587 (1952).
[5] N. Curle, "The influence of solid boundaries upon aerodynamic sound," Proc. R. Soc. A **231**, 505–514 (1955).
[6] J. E. F. Williams, "Hydrodynamic noise," Annu. Rev. Fluid Mech. **1**, 197–222 (1969).
[7] J. E. F. Williams, "Aeroacoustics," Annu. Rev. Fluid Mech. **9**, 447–468 (1977).
[8] J. C. Hardin and D. S. Pope, "An acoustic/viscous splitting technique for computational aeroacoustics," Theor. Comput. Fluid Dyn. **6**, 323–340 (1994).
[9] S. C. Crow, "Aerodynamic sound emission as a singular perturbation problem," Stud. Appl. Math. **49**, 21–46 (1970).
[10] D. G. Crighton, "Basis principles of aerodynamic noise generation," Prog. Aerosp. Sci. **16**, 31–96 (1975).
[11] M. Wang, J. B. Freund, and S. K. Lele, "Computational prediction of flow-generated sound," Annu. Rev. Fluid Mech. **38**, 483–512 (2006).
[12] V. Mantič-Lugo, C. Arratia, and F. Gallaire, "Self-consistent mean flow description of the nonlinear saturation of the vortex shedding in the cylinder wake," Phys. Rev. Lett. **113**, 084501 (2014).
[13] O. Inoue and N. Hatakeyama, "Sound generation by a two-dimensional circular cylinder in a uniform flow," J. Fluid Mech. **471**, 285–314 (2002).
[14] P. G. Drazin and W. H. Reid, *Hydrodynamic Stability* (Cambridge University Press, 2004).
[15] D. Barkley, "Linear analysis of the cylinder wake mean flow," Europhys. Lett. **75**, 750–756 (2006).
[16] B. Pier, "On the frequency selection of finite-amplitude vortex shedding in the cylinder wake," J. Fluid Mech. **458**, 407–417 (2002).
[17] S. Mittal, "Global linear stability analysis of time-averaged flows," Int. J. Numer. Methods Fluids **58**, 111–118 (2008).
[18] V. Mantič-Lugo and F. Gallaire, "Saturation of the response to stochastic forcing in two-dimensional backward-facing step flow: A self-consistent approximation," Phys. Rev. Fluids **1**, 083602 (2016).
[19] D. Sipp and A. Lebedev, "Global stability of base and mean flows: A general approach and its applications to cylinder and open cavity flows," J. Fluid Mech. **593**, 333–358 (2007).
[20] K. Gudmundsson and T. Colonius, "Instability wave models for the near-field fluctuations of turbulent jets," J. Fluid Mech. **689**, 97–128 (2011).
[21] V. Mantič-Lugo, C. Arratia, and F. Gallaire, "A self-consistent model for the saturation dynamics of the vortex shedding around the mean flow in the unstable cylinder wake," Phys. Fluids **27**, 074103 (2015).
[22] S. Beneddine, D. Sipp, A. Arnault, J. Dandois, and L. Lesshafft, "Conditions for validity of mean flow stability analysis," J. Fluid Mech. **798**, 485–504 (2016).
[23] P. R. Amestoy, I. S. Duff, J. Koster, and J.-Y. L'Excellent, "A fully asynchronous multifrontal solver using distributed dynamic scheduling," SIAM J. Matrix Anal. Appl. **23**, 15–41 (2001).
[24] C. W. Rowley, T. Colonius, and A. J. Basu, "On self-sustained oscillations in two-dimensional compressible flow over rectangular cavities," J. Fluid Mech. **455**, 315–346 (2002).
[25] S. Yamouni, D. Sipp, and L. Jacquin, "Interaction between feedback aeroacoustic and acoustic resonance mechanisms in a cavity flow: A global stability analysis," J. Fluid Mech. **717**, 134–165 (2013).
[26] F. Giannetti and P. Luchini, "Structural sensitivity of the first instability of the cylinder wake," J. Fluid Mech. **581**, 167–197 (2007).
[27] Z. Nitzkorski and K. Mahesh, "A dynamic end cap technique for sound computation using the Ffowcs-Williams Hawkings equations," Phys. Fluids **26**, 115101 (2014).
[28] P. Meliga, private communication (2017).